Oxygen impurities link bistability and magnetoresistance in organic spin valves

Ilaria Bergenti[a], *Francesco Borgatti*[a], *Marco Calbucci*[b], *Alberto Riminucci*[a], *Raimondo Cecchini*[c], *Patrizio Graziosi*[a], *Donald MacLaren*[d], *Angelo Giglia*[e], *Jean Pascal Rueff*[f], *Denis Céolin*[f], *Luca Pasquali*[e,g], *Valentin Dediu*[a]

a.CNR-ISMN, via Gobetti 101, 40129 Bologna, Italy

b.Institute of Molecular Science (ICMol) Catedrático José Beltrán Martínez 2 46980 Paterna Spain

c.MDM Laboratory, IMM-CNR, Via C. Olivetti 2, 20864 Agrate Brianza, MB, Italy

d.SUPA, School of Physics and Astronomy, University of Glasgow, Glasgow G12 8QQ

e.IOM-CNR, s.s. 14, Km. 163.5 in AREA Science Park, Basovizza, 34149 Trieste, Italy

f.Synchrotron SOLEIL, Saint-Aubin, BP 48,F-91192 Gif-sur-Yvette Cedex, France

g.Dipartimento di Ingegneria E. Ferrari, Via Vivarelli 10, 41125 Modena, Italy, Department of Physics, University of Johannesburg, P.O. Box 524, Auckland Park 2006, South Africa

KEYWORDS. organic spintronics, spin valve, spin transport, impurity levels, oxygen dopants

ABSTRACT.

Vertical cross-bar devices based on manganite and cobalt injecting electrodes and metal-quinoline molecular transport layer are known to manifest both magnetoresistance and electrical bistability. The two effects are strongly interwoven, inspiring new device applications such as electrical control of the magnetoresistance and magnetic modulation of bistability. To investigate the full device functionality, we first identify the mechanism responsible for electrical switching by associating the electrical conductivity and the impedance behavior with chemical states of buried layers obtained by in operando photoelectron spectroscopy. These measurements revealed that a significant fraction of oxygen ions migrates under voltage application, resulting in a modification of the electronic properties of the organic material and of the oxidation state of the interfacial layer with the ferromagnetic contacts. Variable oxygen doping of the organic molecules represents the key element for correlating bistability and magnetoresistance and our measurements provide the first experimental evidence in favor of the impurity driven model describing the spin transport in organic semiconductors in similar devices.

1. INTRODUCTION

Resistive switching (RS) behavior in organic devices has excited substantial attention because, in addition to the well-known aspects of high performance and low volatility that are inherent to RS memory, the use of organic components would yield easy-to-process, flexible devices.[1] RS has been reported for a wide variety of organic semiconductors including metal quinoline complexes.[2] Typical device configurations are simple and consist of two metallic electrodes sandwiching a semiconducting organic layer; their current–voltage (IV) characteristics show an

hysteresis and their electrical resistance is dependent on the intensity and polarity of a pre-applied "writing" voltage pulse; the resistance change is non-volatile, i.e it persists after the voltage pulse has ended. [1] Recent experiments indicate that, in devices involving spin polarised injectors and metal-quinoline transport layers, in addition to RS, magnetoresistance (MR) occurs.[3-6] Interestingly the two phenomena are strongly correlated: MR can be turned "on" and "off" as well as smoothly tuned between a number of non-volatile states depending on the device resistive state obtaining a full electrical control of MR.[3, 4] This 'multifunctionality' is tantalizing for the development of new devices,[7, 8] with potential applications in multibit nonvolatile data storage and neuromorphic computing.[9, 10] However, the underlying physical mechanisms responsible for the correlation between RS and MR has not yet identified while both effects have been widely explored separately.

Magnetoresistive devices were the subject of numerous investigation worldwide, with some reaching very high MR values [11, 12] and high reproducibility. [13] Investigations of MR in spin valves achieved also important milestones in the field, such as interface controlled functionalities, namely spinterface effects, [14] and quantum control over the statistics of excitons in organic emitting material.[15] Although the spinterface effects shed light on the process of injection of spin polarised carriers from ferromagnetic injectors in organic material [16], a comprehensive theory describing the spin transport in molecular solids and the presence of MR in organic spintronic devices is mostly missing [17].

Hysteretic IV characteristics were observed in a large number of organic materials, from polymers to small molecule ones and are explained either by charging related phenomena or by filament formation phenomena. [1, 18] The former hypothesis is associated with charge-transfer processes in donor-acceptor systems and involves the presence of metallic clusters embedded in

the organic layer,[19] the latter is explained by the formation of locally highly conductive channels (filaments) and is related to redox effects.[20, 21]

In such a complex scenario, the correlation of electrical bistability with MR has obviously created expectations for an additional way of investigating the transport behavior, both for spin and charge properties. Two hypotheses were considered in literature to account for both effects, none of them proven experimentally. In one case it is speculated that MR originates from spin-dependent electron tunneling into highly conductive filamentary paths.[22] Alternatively, a tunnel barrier has been suggested to form [5] at the FM/organic interface, with the barrier being reversibly modified during RS cycles by a redox mechanism, thereby modifying the magnetic injection and producing MR.

In this paper, we focus our attention to the prototypical bistable spin valve device composed of manganite and cobalt spin polarised injectors and a metal-quinoline transport layer. By combining spectroscopic investigations and electrical characterization, we demonstrate that the application of a voltage bias causes oxygen migration within the organic spacer and the reversible modification of the molecule electronic configuration. Experimental evidences link unequivocally the variable oxygen doping of the organic molecule with impurity driven conductivity effects. The MR signal is then interpreted as a result of spin transport in the organic layer across oxygen impurity states. Our investigation provides a key element for the development of a picture of charge-spin effects in organic spintronic devices.

2. EXPERIMENTAL SECTION

Cross bar devices were fabricated with an area of $1mm^2$ and consisted of an thin (10 to 15 nm) Gaq_3 [tris-(8-hydroxyquinoline) Gallium] layer sandwiched between a 20-nm-thick $La_{0.7}Sr_{0.3}MnO_3$ (LSMO) film grown on a $SrTiO_3$ (100) substrate, and a 7-nm-thick Co top

electrode (inset of **Figure1**). An AlO_x tunnel barrier (2nm thick) was deposited between the Gaq_3 and Co layers to minimize the penetration of Co atoms into the organic layer. [23-25] Gaq_3 was considered instead of the well known Alq_3 [26] because it provides similar magnetoelectric behavior, but it allows to decouple the spectroscopic signal originating from the AlO_x barrier and from the organic layer. Samples were prepared *ex-situ* using Channel Spark ablation deposition for LSMO,[27] thermal evaporation for Gaq_3 and Al and electron beam evaporation for Co layer. AlO_x was obtained by exposing the Al layer to a partial pressure of O_2. Transmission electron microscopy (TEM) was employed for structural characterization, using a probe-corrected JEOL ARM200cF instrument that was operated at 200 kV and is equipped with a cold field emission electron gun and a Gatan Quantum electron energy loss spectrometer. Cross-sectional samples were prepared using standard 'lift-out' procedures on an FEI Nova Nanolab Focused Ion Beam instrument and were typically polished to ~100 nm thickness: further thinning tended to damage the delicate organic layer. Electron energy loss spectroscopy (EELS) data were acquired using the spectrum imaging [28] and dual EELS [29] methodologies within Gatan's Digital Micrograph software, which was also used for data processing. Full magnetoresistive characterization was carried out in a 4-point cross bar configuration by using a Keithley 236 SMU in the temperature range 100-300K with a maximum applied field of μH=0.3 T. The LSMO electrode was biased while the Co was kept at ground. Impedance spectra were recorded with an Agilent E4980A LCR-Meter in the 20-100k Hz range in order to distinguish between capacitive and ohmic behavior. Chemical investigation by Hard X-ray Photoelectron Spectroscopy (HAXPES) and X-ray Absorption Spectroscopy (XAS) was performed at room temperature on a sample holder that allows current voltage (I-V) characterization in a 2 point configuration directly within the analysis chamber. The large depth sensitivity achievable by HAXPES (~ 15 nm) and by XAS (~

7 nm) allowed us to investigate deep regions within a working device and to study the effects of the resistive switching on the top electrode, the underlying organic layer and the interfaces with the barrier layer. Devices presented a retention time [7] that greatly surpassed the HAXPES and XAS measurement timescale, ensuring that the observed spectroscopic signatures are unambiguously associated with specific resistance states. XAS measurements were performed across the Co $L_{2,3}$, O-K and C-K absorption edges at the BEAR beamline (Elettra-Trieste). [30] Spectra are acquired in total electron yield mode, by measuring the sample drain current, and they are normalized to the beam flux by using a clean gold sample as reference. HAXPES spectra were collected from the Al1s, C1s, Ga1s, N1s core levels at the GALAXIES beamline (Synchrotron SOLEIL, Paris) [31] using an excitation energy of 7.2KeV. Fits were carried out by XPSpeak software .To eliminate the prospect of oxidation and contamination of the air-exposed side of the Co electrode, all the samples were mildly Ar^+-sputtered (E=500 eV for 30min) in the preparation chamber before spectroscopic investigations. Surface cleanliness was checked by monitoring the surface-sensitive C and O XPS signals. To minimize sample damage under prolonged x-ray exposure, the beam footprint was moved frequently across the device. The XAS simulations were performed on the free Gaq_3 molecule using the transition-potential method using the StoBe DFT simulation code.[32, 33] An IGLO-III basis set was used on each excitation center, while effective core potentials were used for the remaining C atoms. The calculated dipole-excitation spectra were Gaussian convoluted with an energy-dependent broadening and aligned to the experimental curves.

3. RESULTS AND DISCUSSION

Figure 1a shows the typical hysteretic behavior of the current-voltage characteristic, which depends on the polarity of the applied voltage[4] (with respect to the grounded Co top electrode). Initially, devices are in a low resistance state (R_{IRS}(0.1V)~ 25 KΩ) that we call IRS; the I-V characteristic is marked as (1). From the IRS, the device can be set to a high resistance state (HRS) by the application of a sufficiently negative voltage. In Figure 1a the device in the HRS reaches higher R_{HRS}~1MΩ at 0.1 V and is marked as (2). This state is non-volatile and in order to set the device to a low-resistance-state (LRS marked as (3) with R_{LRS}(0.1V) ~5 kΩ at 0.1 V) we must apply a sufficiently positive voltage. In analogy with what was observed in other organic bistable devices [34], our spin valves do not require an electro-forming pulse to enable the bistability. Electro-forming is commonly required in oxide-based RS devices[35] and is usually obtained by the application of a high voltage. As expected,[4] a negative MR is present in the LRS (~8%) which gradually decreases by increasing the resistance of the device (**figure 1b)** eventually eliminating the MR for high enough resistances (1MΩ). Electrical characteristics in our devices are consistent with previous investigations on similar samples[4] and present non linear I-V characteristic [36] [37] [38] with moderate semiconductive behavior (i.e. decreasing resistance with increasing temperature). [39]

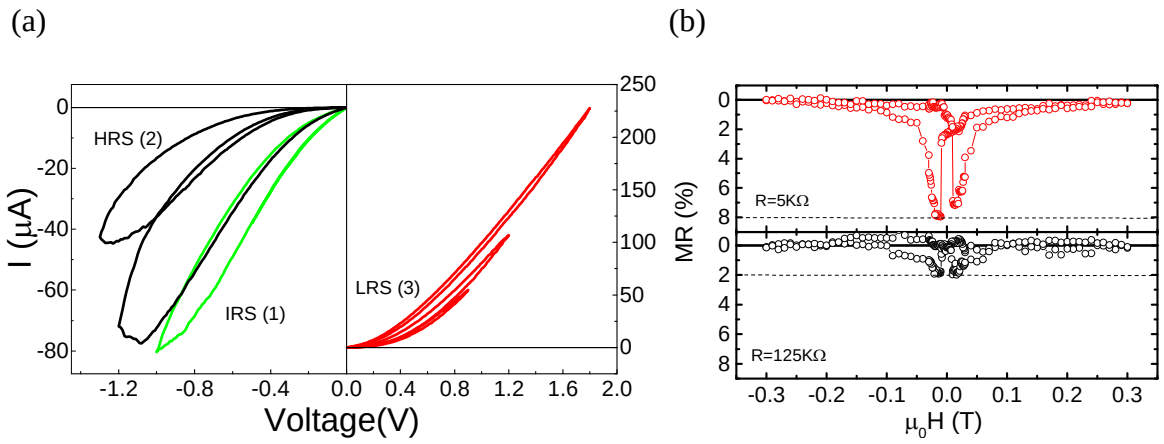

Figure 1 (a) I–V curves of LSMO/ Gaq_3/AlO_x/Co ultra thin device at RT displaying the bistability effect. Inset shows the device structure (b) Negative magnetoresistive response for two different resistive states measured at 100K: LRS (R=5kΩ, MR 8%) and HRS (R=125kΩ, MR 2%) measured at V_{bias}=-0.1V.

To gain insight into the difference in transport between different resistive states, we carried out impedance spectroscopy (V_{AC}=0.01V V_{DC}=-0.1V). The impedance was modeled as a parallel RC loop with a series resistance, R_S (**Figure 2a**).

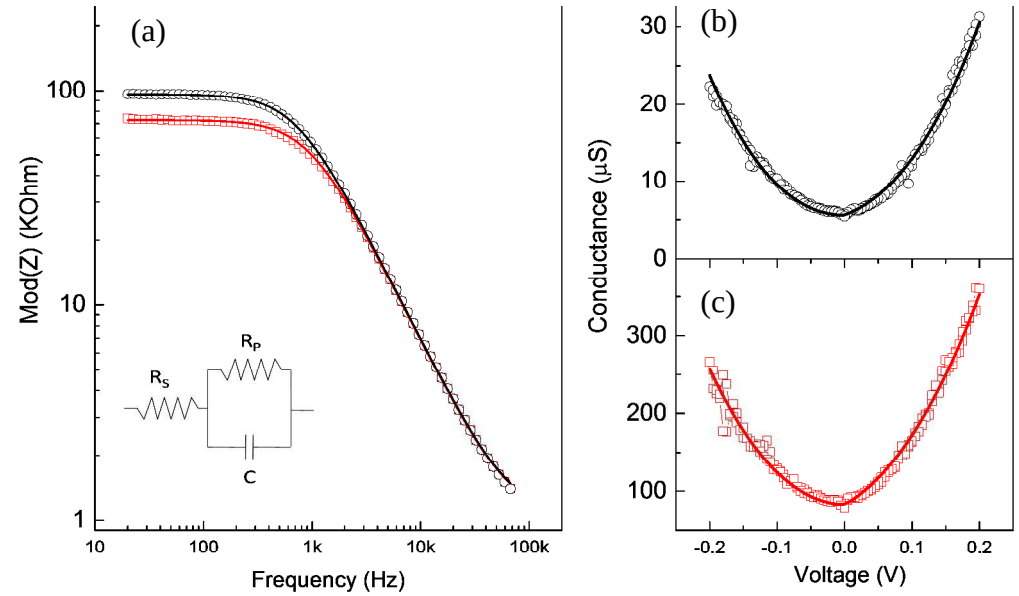

Figure 2 (a)Impedance spectra of two different resistive states. The line is the fit to the equivalent circuit of a R_PC-parallel unit in series with a resistor (R_s). (b) HRS conductance-voltage at 300K. (c) LRS conductance-voltage at 300K The solid lines in b) and c) represent fit to hopping conductance (see SI1)

In each impedance spectrum, the impedance magnitude showed a plateau at low frequencies and decreased above a cut off frequency. Typically, for two different resistive states an almost identical capacitance of C= 2.36 10^{-9}F was found. This value is in agreement with the geometrical value calculated using a relative permittivity of ε_r= 4 as expected for a metal quinoline layer,[40] indicating that the RS was not caused by an extraneous capacitive mechanism at the electrode/organic layer interface and can therefore not be responsible for the conductivity of the individual device states. The series resistance was very low for both states (Rs ~1KΩ) and was attributed to the electrodes whilst the parallel resistance varied during the transition in different resistive states (in Fig 2 from 95kΩ to71kΩ). These results indicate that RS is dominated by the increase of the parallel resistance similarly to other organic based memory devices[41]. The charging effect model can be ruled out to play a major role in RS due to the constant C value [42] while the filamentary mechanism seems the most appropriate to account for the different bulk conductivity of the organic materials. The microscopic origin of filaments is still debated[43] and could also rely to the specific device configuration: some experiments indicate that they are created by the migration of metallic clusters or ions from electrodes onto the organic layer,[21] others involve inhomogeneous conduction of the organic layer itself due to doping or degradation. [44] The differential conductance at low voltage has a nearly parabolic trace for both HRS and LRS, as reported in **Figure 2b**, which excludes conduction by purely metallic filaments, in contrast to the devices described by Gao et al.[45] Our data are therefore consistent with a transport mechanism that involves hopping between localized states forming a preferential path for conductance presumably due to a local modification in the molecular environment. Hopping between localized states is widely regarded as the mode of charge transport that best

describes conduction in organic semiconductors as reported in numerous fundamentals studies.[46] [47, 48] Most works were based on thick organic films and involved a high number of hopping events. At the opposite end, for very thin film, direct tunneling is considered as the dominant mode of transport. Since our devices are made of organic films of intermediate thickness, the approach of Xu *et a*[49], which focusses on transport through a small number of hopping events, is best suited to describe our results (see SI1). Hopping involving up to three localized states fits the experimental data well as shown by continuous line in figure 2b,c. Hopping distances of only a few nanometres are then estimated, indicating that a thinning of the layers' thickness with respect to nominal one should be expected. These results are comparable to those obtained with similar models, such as quantum mechanical multistep tunneling from molecule to molecule[38, 50] or tunneling assisted by via multiple intermediate states[36]

The structure of the device was investigated by TEM and images are presented in **Figure 3**. The TEM images indicate the deposition of LSMO to be of good quality, with a clear epitaxial relationship with the STO substrate. The Gaq_3 layer is amorphous, as expected, and the AlO_x layer is discernable as a uniform, thin band beneath the Co electrode, which is polycrystalline(Figure 3a). EELS signals reveal the clear laminar structure and reveal in particular the oxygen band beneath the top Co electrode that is consistent with the presence of a continuous AlO_x barrier layer (Figure 3b , 3c and SI2).

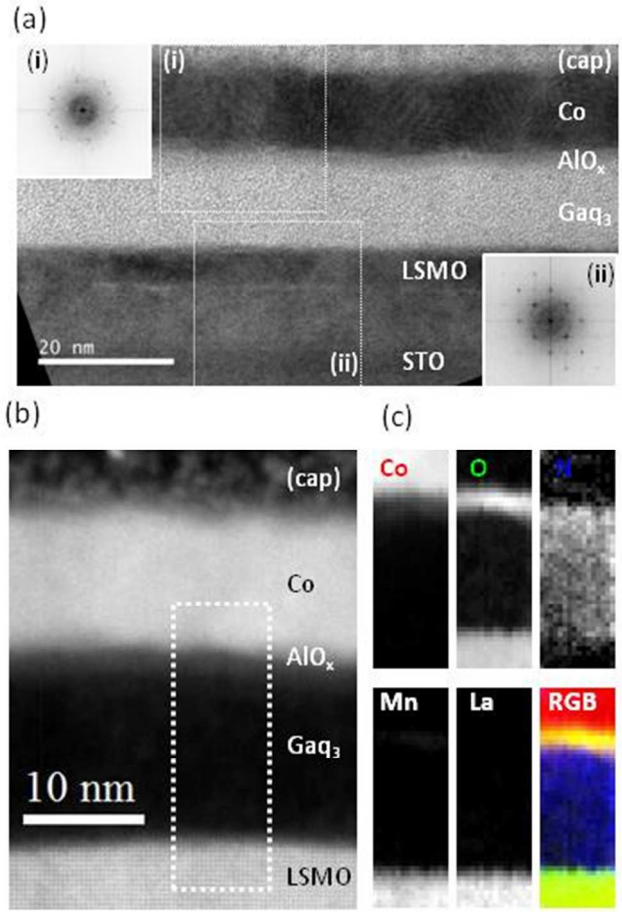

Figure 3 (a) Cross sectional TEM image of a typical device with the layer compositions indicated. Fourier transforms (inset) of the regions labeled (i) and (ii) indicate that the Co layer is polycrystalline and the LSMO and STO have a clear epitaxial relationship. (b)Electron energy loss spectroscopic analysis of a typical device: Dark field STEM image with major layers labeled. Heavier elements appear darkest and the region used for EELS analysis is indicated. (c) Composition maps showing the distribution of elements within the analysed region, each panel indicating the relative strength of background-subtracted EELS signal. The final panel is a red-green-blue composite of the Co, O and N signals.

In operando X-ray Photoelectron Spectroscopy (HAXPES) and X-ray Absorption Spectroscopy (XAS) provide a straightforward evidence of processes setting bistability. XAS spectra of the Co $L_{2,3}$ thresholds are presented in **Figure 4a** and do not reveal significant differences between the HRS and LRS. Both spectra are characteristic of predominantly metallic cobalt and lack pronounced satellite features that would indicate substantial cluster formation [51] or complete oxidation [52], although a weak shoulder is present on the high-energy side of both peaks that suggests the formation of a thin oxide layer, in agreement with the EELS data (SI2).

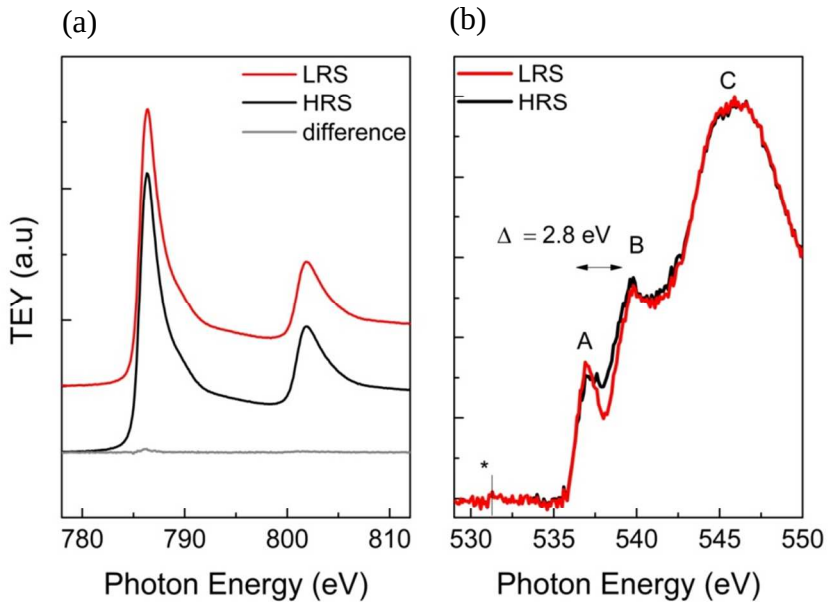

Figure 4(a) X-ray absorption spectra measured across the Co L absorption edge for LRS and HRS. Prior comparison, spectra were normalized by subtraction of a two step-like function with relative height of 2:1 [53]and overall scaling[51] (b) X-ray absorption spectra measured across the O K absorption edge for the HRS and LRS. Asterisk indicates the satellite peak for AlO_x contribution(see SI3); A, B, C are described in the text.

The interpretation of O K-edge spectra, shown in **figure 4b**, is more complex because contributions arise from both AlO_x and Gaq_3 layers but an important result is that there are clear changes between the HRS and LRS. The spectra are dominated by a broad peak centered at *E*=546 eV (labeled 'C') and there are two satellites, at *E*= 539.8 eV ('B') and *E*= 537 eV ('A'). Previous studies of amorphous AlO_x layers [54] and Gaq_3 [55, 56] allow feature A to be attributed to AlO_x (see SI3). Recent paper [57] on AlO_x based RS devices uses the sharpness of this satellite peak as an indicator of the presence of oxygen vacancies. Indeed, it has been noted elsewhere that AlO_x tunnel layers formed by the oxidation of aluminum thin films incorporate O_2^- ions that are weakly bound to the positively charged oxygen vacancies but are able to drift into and out of the barrier layer under electrical bias.[58] In this framework, the LRS, set after the application of a positive bias to the LSMO layer, would rely on the migration of negative charges (O_2^- included) towards the LSMO layer, leaving defective $AlO_{x.}$ Oxygen represents a source of doping in our samples because the preparation of the tunnel barrier included O_2 exposure, in addition to brief exposure to the atmosphere before characterization.[59]

To study in more detail the role of the AlO_x layer in RS, we analyzed the Al chemical state directly by photoemission spectroscopy, as this allows direct isolation of the contribution of AlO_x. The HAXPES Al1s spectra shown in **figure 5a** are typically described by three components [25]: a main peak corresponding to the AlO_x contribution[60] with two satellites at ΔE_1= +1.7 eV and ΔE_2= -2.5 eV. The lower binding energy contribution is associated with the metallic Al (Al-Al) while the broader contribution could be related to the higher oxidation states for Al, as for example Al_2O_3.[60] The HRS and LRS spectra indicate a subtle shift, relative to the IRS, of the main Al1s component only, which shifts by + (-) 0.1 eV for the H(L)RS, with a slightly broader lineshape (Γ=1.8). An Al1s core level shift to higher (lower) binding energy indicates a

higher (lower) oxidation state,[61] indicating that in the HRS the Al experiences increased oxygenation and a slightly more inhomogeneous chemical environment. The increase of oxygenation in HRS is confirmed by the relative percentage of the peak associated to the AlO_x with respect to the total area that is 78% while in LRS is 74%. (See **Table 1**)

	Assignement	Energy (eV)	FWHM (eV)	Peak area (%)
IRS	AlO_x	1561.2	1.7	62.0 %
	Al-Al	1558.6	2.5	14.5%
HRS	AlO_x	1561.3	1.8	78.0%
	Al-Al	1558.6	2.0	5.5%
LRS	AlO_x	1561.1	1.6	74.0%
	Al-Al	1558.6	3.1	8.1%

Tab 1 Al 1s assignments for AlO_x and metallic Al and the relative contribution to the total peak area in the three resistive states. Each contribution is fitted by using a Guassian line shape.

Both O K-edge and Al1s analysis indicate a difference in the Al oxidation state between the LRS and HRS. We propose that the HRS, set by the application of a negative bias to the LSMO contact, is obtained by trapping of O_2^- in the AlO_X layer while the LRS, set by the application of positive bias to the LSMO contact, is obtained after migration of O_2^- away from the AlO_x. In the HRS, oxygen migration is not associated with any evident change in the Co layer (as observed in HAXPES), indicating that the AlO_x tunnel barrier is the principal oxygen trapping layer.

We turn now to the organic molecule. It is well established from theoretical calculations [62, 63] that in metal quinoline complexes the highest occupied molecular orbital (HOMO) is located on the phenoxideside of the quinolinol ligands, whereas the lowest unoccupied molecular orbital (LUMO) is found on the pyridyl side; the central metal ion (Ga) contributes negligibly to the density of states (DOS). Thus, it may be expected that any possible variations to the electronic configuration of the molecule during RS are most likely to produce a sizeable effect on the N1s or C1s HAXPES spectra. The C1s core levels HAXPES spectra for IRS, HRS and LRS are shown in **figure 5b**.

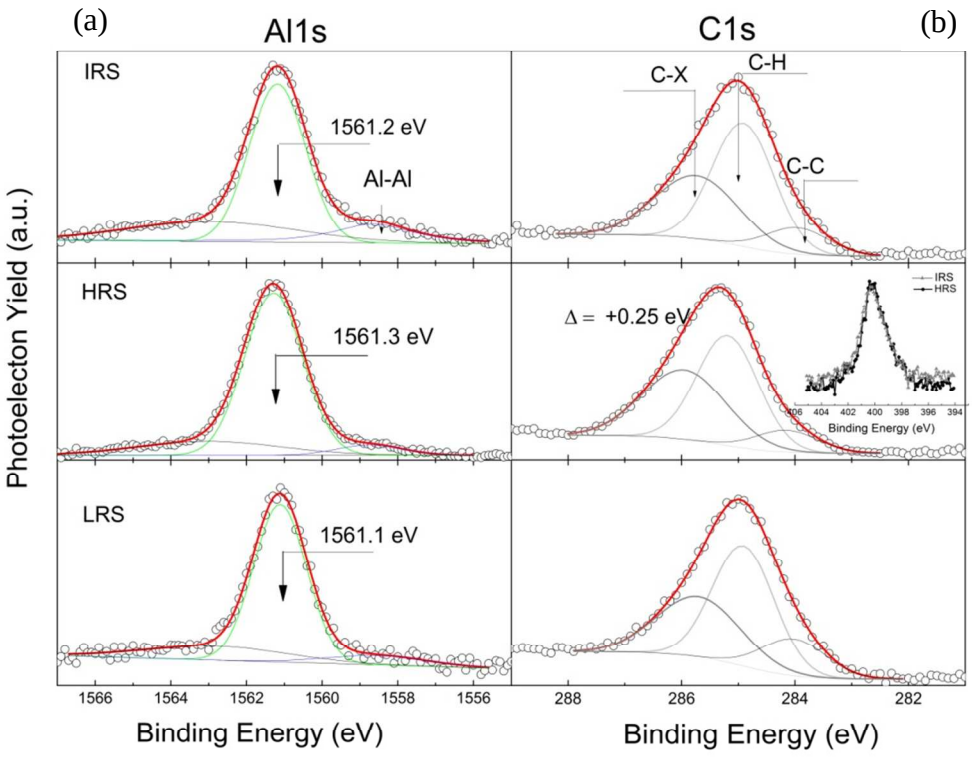

Figure 5 (a) Normalized HAXPES Al 1s spectra (open circles) for the IRS (top), HRS(intermediate) and LRS(bottom). Green and grey lines represent the three components and red lines the curve fit. (b) Normalized HAXPES C1s spectra (open circles) for IRS, HRS and

LRS. Lines represent the three components and red lines the curve fit. Inset: HAXPES N1s spectra for IRS and HRS

They results from three main components corresponding to three bonding environments for carbon in the structure of the 8-quinolinol ligand (C–C bonds, C–H bonds, and C–X bonds where X stands for oxygen or nitrogen) and it is consistent with previous investigations [25] of similar samples. During the fitting process, the area ratio for the C–C, C–H, and C–X components was kept 1:3:5, in agreement with their ratios in the complex. The binding energies of all three components do not change between the IRS and the LRS but in the HRS increase by 0.25 eV, which is generally a signature of an oxidation process (i.e. removal of electronic charge). Nevertheless, it is worth noting that a shift of C1s binding energy concurrent with a broadening of the N1s peak during deposition of Ca onto Alq3 has previously been attributed to charge donation and ligand dissociation. [64] In our case we did not observe any change in the N1s peak between the IRS and HRS (inset to Figure 5), excluding such effects. We therefore interpret the increase in C1s binding energy as a consequence of ionization of the molecule to form an Alq3 cation. This charge removal is reversible, since the HRS and LRS were cycled many times without changing their spectroscopic signatures. This picture is supported by an analysis of the XAS C-K-edge spectra shown in **figure 6**. XAS spectra relates to unoccupied states (in the presence of a core hole), as they reflect dipole-allowed transitions to empty molecular orbitals. HRS spectra are narrower than the corresponding LRS spectra, indicating an overall difference in the lower lying empty states. Figure 6a shows the calculated C K-edge spectra for the Gaq_3 molecule in its neutral form and after the removal of an electronic charge (Gaq_3 cation). Calculated spectra are in agreement with previous investigations [62, 65] of bulk metal quinoline

and feature more structured contributions with respect to experimental data, indicating that extrinsic broadening due to complex molecular configuration is expected to dominate in devices. By a qualitative comparison of the measured and calculated spectra in neutral and positively charged states, the narrower experimental lineshape of the broad feature centered at 289 eV in HRS indicates a partial presence of a Gaq_3 cations.

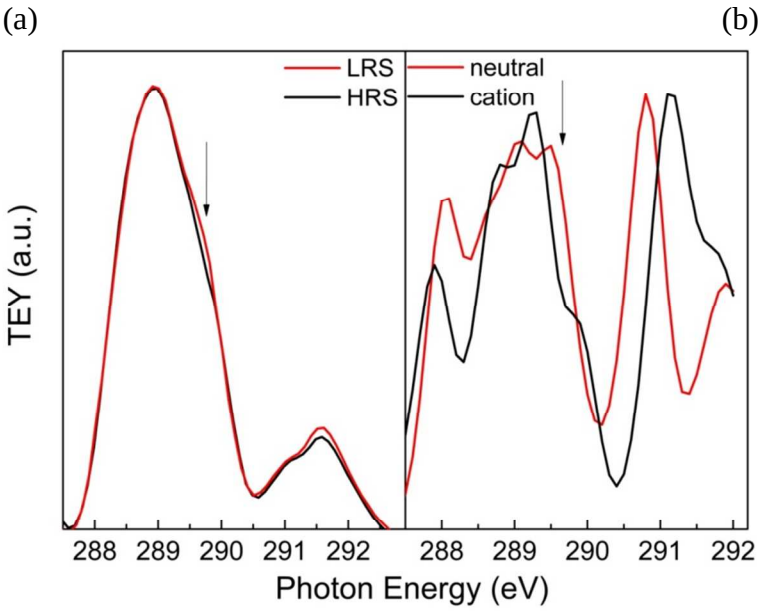

Figure 6 (a) X-ray absorption spectra measured across the C K absorption edge. (b)Calculated C K edge absorption spectra for neutral Gaq_3 molecule and for Gaq_3 cation obtained by a removal of an electronic charge.

Considering the Oxygen drift in and out the barrier, the reversible generation of positively charged states in Gaq_3 is then interpreted as a results of the formation of a charge-transfer complex involving the organic molecule and molecular oxygen. [66, 67] A partial redistribution of

the electronic charge within the complex yields then a negatively charged oxygen molecule and a hole on the quinoline ligand. [68]

The positive charging of the organic molecules, modifying their electronic structure,[69, 70] results in a higher localization of electrons in the HOMO with respect to the neutral and negatively charged quinoline molecule. This localization of the HOMO would be unfavorable for electron hopping to a neighboring molecule and thus unfavorable for electron transport, as expected for HRS.[69] We stress that XAS and HAXPES spectroscopic investigations average all over the sample probing volume and thus changes of the electronic configuration of organic layer are not restricted to local conduction paths as expected in filamentary conduction process but involves all the organic molecules down to few nanometer from the interface with the AlO_x layer.

A schematic of the underlying physical processes during RS is presented in **figure 7**. The HRS is set by the application of a negative voltage to the LSMO: negative charges, including free electrons and O_2^- drift towards the Co top electrode. AlO_x then gets oxidized and acts as a trap, blocking the O_2^- ions and preventing interaction with Co. The oxygen drift is accompanied by a positive charging of the organic molecules, modifying the Gaq_3 electronic configuration:[69] charges are generally more localized inside the individual quinoline unit inhibiting the electron transport and causing a subsequent increase of overall resistivity. In switching to the LRS by the application of a positive voltage to LSMO, oxygen migrates towards the LSMO layer to leave a defective AlO_x barrier and restore the neutrality of the Gaq_3 molecule. Once established that resistive switching is associated to oxygen migration across the organic layer and to a reversible formation of Gaq_3 cations, we discuss the correlation with MR.

An important issue to take into account is the voltage regime at which bistability and MR are found. While bistability is set by applying few V to our device, MR is detectable only at small voltages (well below 1 V) which are lower than interfacial electronic barriers for the charge injection into HOMO or LUMO level.[71] Such peculiar MR voltage dependence together with the absence of Hanle effect [72] expected in case of HOMO-LUMO transport, pushed several authors [12, 36] to propose a qualitatively different picture to describe spin transport in the OSVs based on the presence of intragap localized levels.

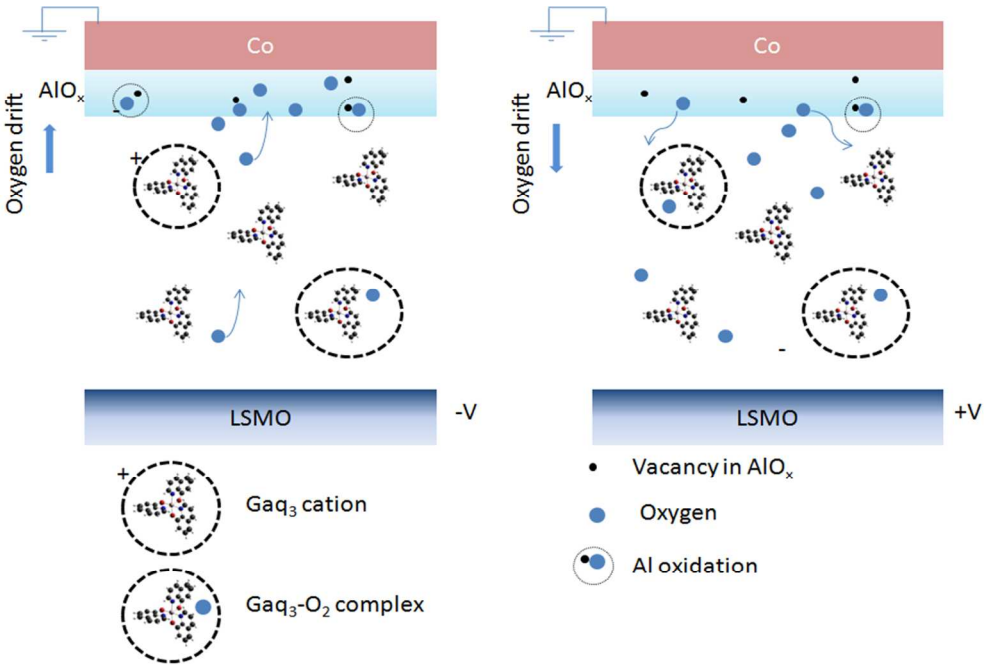

Figure 7 Schematic representation of RS: HRS (left) and LRS (right). HRS is set by the application of a negative voltage to the LSMO: negative charges, including free electrons and O_2^- drift towards the Co top electrode. The AlO_x is oxidized and acts as trap, blocking the O_2^- ions and preventing interaction with Co. The oxygen drift is accompanied by a positive charging of

the organic molecules. Switching to the LRS, oxygen migrates towards the LSMO layer to leave a defective AlO_x barrier and restore the neutrality of the Gaq_3 molecule.

In our case, the MR intensity depends on the specific resistive state in which the device is put: on the basis of results above, MR is absent when a more efficient insulating AlO_x barrier is set and Gaq_3 cations are formed, while MR has its maximum value in case of defective AlO_x barrier and after oxygen ions migration into the organic layer and the formation of complexes. We expect then that AlO_x defective barrier [73] will generate a number of localized states able to promote the spin injection from the Cobalt electrode into the organic layer where the spin transport takes place in presence of Oxygen ions acting as dopant (or impurity), via the formation of complexes with Gaq_3. Our data are consistent with the formation of intragap impurity levels to describe spin and charge transport in our spin valves. Recently a model based on tunneling onto an impurity band located in the gap between molecular orbitals [74] was proposed to explain MR in thick devices, but its experimental validation has yet to be accomplished.

The decrease of MR corresponds to more efficient insulating AlOx barrier,[73] that limits the tunneling into the organic layer, and to a lower density of impurities that in association with electronic localization of Gaq_3 cations increases the residence time of spin/charges, which have the effect of enhancing spin dephasing processes.[75]

Oxygen as dopant in organics can in principle originate from intrinsic doping during deposition. Interestingly, among devices presenting reproducible MR in literature most of them have the LSMO oxide[13, 39, 76] as electrode or include the presence of oxide tunnel tunnel barrier [37, 77-79] indicating the oxide layers as most plausible sources of oxygens in such devices. Recently Grünewald *et al.*[5], discussing similar devices, advanced a model ascribing both the resistive

switching and magnetic characteristics uniquely to oxygen variations in the LSMO electrode. [80] Our set of data do not access the interfacial LSMO layer in reason of the limited electron escape depth for Hard X-Ray photoemission, providing little access to the deep buried interface with LSMO layer. Nevertheless, our data provide a complementary interpretation of the mechanism, indicating significant modifications of the stoichiometry of the aluminum oxide barrier and substantial oxygen diffusion inside the organic layer, both factors controlling the device resistance.

4. CONCLUSIONS

In summary, we have demonstrated that resistive switching effect in LSMO/Gaq_3/AlO_x/Co devices is driven by the oxygen migration across the structure: both AlOx tunnel barrier and Gaq_3 layer reversibly change the oxygen concentrations while switching between the high and the low resistive states. The reversible shift of the C peak by the programming voltage indicates that the oxygenated organic layer is a key element for establishing both the bistability and magnetoresistance behaviors, although at this stage it is difficult to separate quantitatively the roles of Gaq_3 and AlO_x layers. These findings shed important light on the still unidentified mechanism of magnetoresistance and represent the first experimental evidence in support of the role of intragap impurity levels in the spin-charge conduction in this class of devices.

Supporting Information

Supporting file contains:

SI1:analysis of voltage dependence of the hopping conductance

SI2:Details of EELS analysis

SI3: Supporting data for O Kedge XAS interpretation:

.

AUTHOR INFORMATION

Corresponding Author

*Phone:+39 0516398509 Fax:+39 0516398540 mail: ilaria.bergenti@cnr.it

Author Contributions

The manuscript was written through contributions of all authors. All authors have given approval to the final version of the manuscript

Funding Sources

This work is funded through the European Union Seventh Framework Programme (FP7/2007-2013) under grant agreement GA No. 263104 and COST action 15128. We thank SOLEIL and ELETTRA synchrotrons for provision of synchrotron radiation facilities at beamline GALAXIES (proposal number 20130329) and beamline BEAR (proposal number 20135188) respectively.

REFERENCES

1. Scott, J. C.; Bozano, L. D., Nonvolatile Memory Elements Based on Organic Materials. *Advanced Materials* **2007,** *19* (11), 1452-1463.

2. Tu, C.-H.; Lai, Y.-S.; Dim-Lee, K., Memory effect in the current-voltage characteristic of 8-hydroquinoline aluminum salt films. *Electron Device Letters, IEEE* **2006,** *27* (5), 354-356.

3. Hueso, L. E.; Bergenti, I.; Riminucci, A.; Zhan, Y. Q.; Dediu, V., Multipurpose Magnetic Organic Hybrid Devices. *Advanced Materials* **2007,** *19* (18), 2639-2642.

4. Prezioso, M.; Riminucci, A.; Bergenti, I.; Graziosi, P.; Brunel, D.; Dediu, V. A., Electrically Programmable Magnetoresistance in Multifunctional Organic-Based Spin Valve Devices. *Advanced Materials* **2011,** *23* (11), 1371-1375.

5. Grünewald, M.; Homonnay, N.; Kleinlein, J.; Schmidt, G., Voltage-controlled oxide barriers in organic/hybrid spin valves based on tunneling anisotropic magnetoresistance. *Physical Review B* **2014,** *90* (20), 205208.

6. Dediu, V.; Hueso, L. E.; Bergenti, I.; Riminucci, A.; Borgatti, F.; Graziosi, P.; Newby, C.; Casoli, F.; De Jong, M. P.; Taliani, C.; Zhan, Y., Room-temperature spintronic effects in Alq_3-based hybrid devices. *Physical Review B* **2008,** *78* (11), 115203.

7. Prezioso, M.; Riminucci, A.; Graziosi, P.; Bergenti, I.; Rakshit, R.; Cecchini, R.; Vianelli, A.; Borgatti, F.; Haag, N.; Willis, M.; Drew, A. J.; Gillin, W. P.; Dediu, V. A., A Single-Device Universal Logic Gate Based on a Magnetically Enhanced Memristor. *Advanced Materials* **2013,** *25* (4), 534-538.

8. Sangwan, V. K.; Jariwala, D.; Kim, I. S.; Chen, K.-S.; Marks, T. J.; Lauhon, L. J.; Hersam, M. C., Gate-tunable memristive phenomena mediated by grain boundaries in single-layer MoS2. *Nat Nano* **2015,** *10* (5), 403-406.

9. Krzysteczko, P.; Münchenberger, J.; Schäfers, M.; Reiss, G.; Thomas, A., The Memristive Magnetic Tunnel Junction as a Nanoscopic Synapse-Neuron System. *Advanced Materials* **2012,** *24* (6), 762-766.

10. Zhang, K.; Cao, Y.-l.; Fang, Y.-w.; Li, Q.; Zhang, J.; Duan, C.-g.; Yan, S.-s.; Tian, Y.-f.; Huang, R.; Zheng, R.-k.; Kang, S.-s.; Chen, Y.-x.; Liu, G.-l.; Mei, L.-m., Electrical control of

memristance and magnetoresistance in oxide magnetic tunnel junctions. *Nanoscale* **2015,** *7* (14), 6334-6339.

11. Sun, D.; Yin, L.; Sun, C.; Guo, H.; Gai, Z.; Zhang, X. G.; Ward, T. Z.; Cheng, Z.; Shen, J., Giant Magnetoresistance in Organic Spin Valves. *Physical Review Letters* **2010,** *104* (23), 236602.

12. Barraud, C.; Seneor, P.; Mattana, R.; Fusil, S.; Bouzehouane, K.; Deranlot, C.; Graziosi, P.; Hueso, L.; Bergenti, I.; Dediu, V.; Petroff, F.; Fert, A., Unravelling the role of the interface for spin injection into organic semiconductors. *Nat Phys* **2010,** *6* (8), 615-620.

13. Xiong, Z. H.; Wu, D.; Valy Vardeny, Z.; Shi, J., Giant magnetoresistance in organic spin-valves. *Nature* **2004,** *427* (6977), 821-824.

14. Cinchetti, M.; Dediu, V. A.; Hueso, L. E., Activating the molecular spinterface. *Nature Materials* **2017,** *16,* 507.

15. Prieto-Ruiz, J. P. M., S.G.; Prima-García,H.; Riminucci,A.; Graziosi,P.; Cinchetti,M.; Aeschlimann,M.; Dediu,V. A.; Coronado, E. , Controlling singlet-triplet ratio in OLEDs by spin polarised currents. *arXiv:1612.00633v1* **2016**.

16. Steil, S.; Großmann, N.; Laux, M.; Ruffing, A.; Steil, D.; Wiesenmayer, M.; Mathias, S.; Monti, O. L. A.; Cinchetti, M.; Aeschlimann, M., Spin-dependent trapping of electrons at spinterfaces. *Nature Physics* **2013,** *9,* 242.

17. Dediu, V. A.; Riminucci, A., More than spectroscopy. *Nature Nanotechnology* **2013,** *8,* 885.

18. Lee, P.-T.; Chang, T.-Y.; Chen, S.-Y., Tuning of the electrical characteristics of organic bistable devices by varying the deposition rate of Alq3 thin film. *Organic Electronics* **2008,** *9* (5), 916-920.

19. Chu, C. W.; Ouyang, J.; Tseng, J. H.; Yang, Y., Organic Donor–Acceptor System Exhibiting Electrical Bistability for Use in Memory Devices. *Advanced Materials* **2005,** *17* (11), 1440-1443.

20. Cölle, M.; Büchel, M.; de Leeuw, D. M., Switching and filamentary conduction in non-volatile organic memories. *Organic Electronics* **2006,** *7* (5), 305-312.

21. Busby, Y.; Nau, S.; Sax, S.; List-Kratochvil, E. J. W.; Novak, J.; Banerjee, R.; Schreiber, F.; Pireaux, J.-J., Direct observation of conductive filament formation in Alq3 based organic resistive memories. *Journal of Applied Physics* **2015,** *118* (7), 075501.

22. Li, B.; Yoo, J.-W.; Kao, C.-Y.; Jang, H. W.; Eom, C.-B.; Epstein, A. J., Electrical bistability and spin valve effect in a ferromagnet/organic semiconductor/ferromagnet heterojunction. *Organic Electronics* **2010,** *11* (6), 1149-1153.

23. Zhan, Y. Q.; Liu, X. J.; Carlegrim, E.; Li, F. H.; Bergenti, I.; Graziosi, P.; Dediu, V.; Fahlman, M., The role of aluminum oxide buffer layer in organic spin-valves performance. *Applied Physics Letters* **2009,** *94* (5), 053301.

24. Sidorenko, A. A.; Pernechele, C.; Lupo, P.; Ghidini, M.; Solzi, M.; De Renzi, R.; Bergenti, I.; Graziosi, P.; Dediu, V.; Hueso, L.; Hindmarch, A. T., Interface effects on an ultrathin Co film in multilayers based on the organic semiconductor Alq3. *Applied Physics Letters* **2010,** *97* (16), 162509.

25. Borgatti, F.; Bergenti, I.; Bona, F.; Dediu, V.; Fondacaro, A.; Huotari, S.; Monaco, G.; MacLaren, D. A.; Chapman, J. N.; Panaccione, G., Understanding the role of tunneling barriers in organic spin valves by hard x-ray photoelectron spectroscopy. *Applied Physics Letters* **2010,** *96* (4), 043306.

26. Droghetti, A.; Steil, S.; Großmann, N.; Haag, N.; Zhang, H.; Willis, M.; Gillin, W. P.; Drew, A. J.; Aeschlimann, M.; Sanvito, S.; Cinchetti, M., Electronic and magnetic properties of the interface between metal-quinoline molecules and cobalt. *Physical Review B* **2014,** *89* (9), 094412.

27. Graziosi, P.; Prezioso, M.; Gambardella, A.; Kitts, C.; Rakshit, R. K.; Riminucci, A.; Bergenti, I.; Borgatti, F.; Pernechele, C.; Solzi, M.; Pullini, D.; Busquets-Mataix, D.; Dediu, V. A., Conditions for the growth of smooth La0.7Sr0.3MnO3 thin films by pulsed electron ablation. *Thin Solid Films* **2013,** *534*, 83-89.

28. Hunt, J. A.; Williams, D. B., Electron energy-loss spectrum-imaging. *Ultramicroscopy* **1991,** *38* (1), 47-73.

29. Scott, J.; Thomas, P. J.; MacKenzie, M.; McFadzean, S.; Wilbrink, J.; Craven, A. J.; Nicholson, W. A. P., Near-simultaneous dual energy range EELS spectrum imaging. *Ultramicroscopy* **2008,** *108* (12), 1586-1594.

30. Nannarone, S.; Borgatti, F.; DeLuisa, A.; Doyle, B. P.; Gazzadi, G. C.; Giglia, A.; Finetti, P.; Mahne, N.; Pasquali, L.; Pedio, M.; Selvaggi, G.; Naletto, G.; Pelizzo, M. G.; Tondello, G., The BEAR Beamline at Elettra. *AIP Conference Proceedings* **2004,** *705* (1), 450-453.

31. Rueff, J.-P.; Ablett, J. M.; Ceolin, D.; Prieur, D.; Moreno, T.; Baledent, V.; Lassalle-Kaiser, B.; Rault, J. E.; Simon, M.; Shukla, A., The GALAXIES beamline at the SOLEIL synchrotron: inelastic X-ray scattering and photoelectron spectroscopy in the hard X-ray range. *Journal of Synchrotron Radiation* **2015,** *22* (1), 175-179.

32. Hermann, K.; Pettersson, L. G. M.; Casida, M. E.; Daul, C.; Goursot, A.; Koester, A.; Proynov, E.; St-Amant, A.; Salahub, D. R.; Carravetta, V. *StoBe-deMon version 3.0*, 2007.

33. Triguero, L.; Pettersson, L. G. M.; Ågren, H., Calculations of near-edge x-ray-absorption spectra of gas-phase and chemisorbed molecules by means of density-functional and transition-potential theory. *Physical Review B* **1998,** *58* (12), 8097-8110.

34. Bozano, L. D.; Kean, B. W.; Deline, V. R.; Salem, J. R.; Scott, J. C., Mechanism for bistability in organic memory elements. *Applied Physics Letters* **2004,** *84* (4), 607-609.

35. Waser, R.; Aono, M., Nanoionics-based resistive switching memories. *Nat Mater* **2007,** *6* (11), 833-840.

36. Tran, T. L. A.; Le, T. Q.; Sanderink, J. G. M.; van der Wiel, W. G.; de Jong, M. P., The Multistep Tunneling Analogue of Conductivity Mismatch in Organic Spin Valves. *Advanced Functional Materials* **2012,** *22* (6), 1180-1189.

37. Schoonus, J. J. H. M.; Lumens, P. G. E.; Wagemans, W.; Kohlhepp, J. T.; Bobbert, P. A.; Swagten, H. J. M.; Koopmans, B., Magnetoresistance in Hybrid Organic Spin Valves at the Onset of Multiple-Step Tunneling. *Physical Review Letters* **2009,** *103* (14), 146601.

38. Lin, R.; Wang, F.; Rybicki, J.; Wohlgenannt, M.; Hutchinson, K. A., Distinguishing between tunneling and injection regimes of ferromagnet/organic semiconductor/ferromagnet junctions. *Physical Review B* **2010,** *81* (19), 195214.

39. Jiang, S. W.; Shu, D. J.; Lin, L.; Shi, Y. J.; Shi, J.; Ding, H. F.; Du, J.; Wang, M.; Wu, D., Strong asymmetrical bias dependence of magnetoresistance in organic spin valves: the role of ferromagnetic/organic interfaces. *New Journal of Physics* **2014,** *16*.

40. Berleb, S.; Brütting, W., Dispersive Electron Transport in tris(8-Hydroxyquinoline) Aluminum (Alq3) Probed by Impedance Spectroscopy. *Physical Review Letters* **2002,** *89* (28), 286601.

41. Sebastian, P.; Lindner, F.; Walzer, K.; Lüssem, B.; Leo, K., Investigation on the origin of the memory effect in metal/organic semiconductor/metal structures. *Journal of Applied Physics* **2011,** *110* (8), 084508.

42. Nau, S.; Sax, S.; List-Kratochvil, E. J. W., Unravelling the Nature of Unipolar Resistance Switching in Organic Devices by Utilizing the Photovoltaic Effect. *Advanced Materials* **2014,** *26* (16), 2508-2513.

43. Cho, B.; Song, S.; Ji, Y.; Kim, T.-W.; Lee, T., Organic Resistive Memory Devices: Performance Enhancement, Integration, and Advanced Architectures. *Advanced Functional Materials* **2011,** *21* (15), 2806-2829.

44. Pender, L. F.; Fleming, R. J., Memory switching in glow discharge polymerized thin films. *Journal of Applied Physics* **1975,** *46* (8), 3426-3431.

45. Gao, S.; Song, C.; Chen, C.; Zeng, F.; Pan, F., Dynamic Processes of Resistive Switching in Metallic Filament-Based Organic Memory Devices. *The Journal of Physical Chemistry C* **2012,** *116* (33), 17955-17959.

46. Tessler, N.; Preezant, Y.; Rappaport, N.; Roichman, Y., Charge Transport in Disordered Organic Materials and Its Relevance to Thin-Film Devices: A Tutorial Review. *Advanced Materials* **2009,** *21* (27), 2741-2761.

47. Coropceanu, V.; Cornil, J.; da Silva, D. A.; Olivier, Y.; Silbey, R.; Bredas, J. L., Charge transport in organic semiconductors. *Chemical Reviews* **2007,** *107* (4), 926-952.

48. Bässler, H.; Köhler, A., Charge Transport in Organic Semiconductors. In *Unimolecular and Supramolecular Electronics I: Chemistry and Physics Meet at Metal-Molecule Interfaces*, Metzger, R. M., Ed. Springer Berlin Heidelberg: Berlin, Heidelberg, 2012; pp 1-65.

49. Xu, Y.; Ephron, D.; Beasley, M. R., Directed inelastic hopping of electrons through metal-insulator-metal tunnel junctions. *Physical Review B* **1995,** *52* (4), 2843-2859.

50. Gobbi, M.; Golmar, F.; Llopis, R.; Casanova, F.; Hueso, L. E., Room-Temperature Spin Transport in C60-Based Spin Valves. *Advanced Materials* **2011,** *23* (14), 1609-1613.

51. Cheng, P.-Y.; Chiang, M.-R.; Chan, Y.-L.; Hsu, Y.-J.; Wang, P.-C.; Wei, D. H., Deep Co penetration and spin-polarization of C60 molecules at hybridized Co-C60 interfaces. *Applied Physics Letters* **2014,** *104* (4), 043303.

52. Telling, N. D.; van der Laan, G.; Ladak, S.; Hicken, R. J.; Arenholz, E., Evidence of a barrier oxidation dependence on the interfacial magnetism in Co/alumina based magnetic tunnel junctions. *Journal of Applied Physics* **2006,** *99* (8), 08E505.

53. Wang, Z. L.; Bentley, J.; Evans, N. D., Valence state mapping of cobalt and manganese using near-edge fine structures. *Micron* **2000,** *31* (4), 355-362.

54. Århammar, C.; Pietzsch, A.; Bock, N.; Holmström, E.; Araujo, C. M.; Gråsjö, J.; Zhao, S.; Green, S.; Peery, T.; Hennies, F.; Amerioun, S.; Föhlisch, A.; Schlappa, J.; Schmitt, T.; Strocov, V. N.; Niklasson, G. A.; Wallace, D. C.; Rubensson, J.-E.; Johansson, B.; Ahuja, R., Unveiling the complex electronic structure of amorphous metal oxides. *Proceedings of the National Academy of Sciences* **2011,** *108* (16), 6355-6360.

55. Yokoyama, T.; Ishii, H.; Matsuie, N.; Kanai, K.; Ito, E.; Fujimori, A.; Araki, T.; Ouchi, Y.; Seki, K., Neat Alq3 thin film and metal/Alq3 interfaces studied by NEXAFS spectroscopy. *Synthetic Metals* **2005,** *152* (1), 277-280.

56. Fang, S.; Pang, Z.; Du, Y.; Zheng, L.; Zhang, X.; Wang, F.; Yuan, H.; Han, S., The structure of Mn-doped tris(8-hydroxyquinoline)gallium by extended x-ray absorption fine

structure spectroscopy and first principles calculations. *Journal of Applied Physics* **2012,** *112* (11), 113519.

57. Nigo, S.; Kubota, M.; Harada, Y.; Hirayama, T.; Kato, S.; Kitazawa, H.; Kido, G., Conduction band caused by oxygen vacancies in aluminum oxide for resistance random access memory. *Journal of Applied Physics* **2012,** *112* (3), 033711.

58. Tan, E.; Mather, P. G.; Perrella, A. C.; Read, J. C.; Buhrman, R. A., Oxygen stoichiometry and instability in aluminum oxide tunnel barrier layers. *Physical Review B* **2005,** *71* (16), 161401.

59. Laubender, J.; Chkoda, L.; Sokolowski, M.; Umbach, E., The influence of oxygen and air on the characteristics of organic light-emitting devices studied by in vacuo measurements. *Synthetic Metals* **2000,** *111–112*, 373-376.

60. Risterucci, P.; Renault, O.; Zborowski, C.; Bertrand, D.; Torres, A.; Rueff, J. P.; Ceolin, D.; Grenet, G.; Tougaard, S., Effective inelastic scattering cross-sections for background analysis in HAXPES of deeply buried layers. *Applied Surface Science* **2017,** *402*, 78-85.

61. Kottler, V.; Gillies, M. F.; Kuiper, A. E. T., An in situ x-ray photoelectron spectroscopy study of AlOx spin tunnel barrier formation. *Journal of Applied Physics* **2001,** *89* (6), 3301-3306.

62. Curioni, A.; Andreoni, W.; Treusch, R.; Himpsel, F. J.; Haskal, E.; Seidler, P.; Heske, C.; Kakar, S.; van Buuren, T.; Terminello, L. J., Atom-resolved electronic spectra for Alq3 from theory and experiment. *Applied Physics Letters* **1998,** *72* (13), 1575-1577.

63. Bisti, F.; Stroppa, A.; Donarelli, M.; Picozzi, S.; Ottaviano, L., Electronic structure of tris(8-hydroxyquinolinato)aluminium(III) revisited using the Heyd-Scuseria-Ernzerhof hybrid functional: Theory and experiments. *Physical Review B* **2011,** *84* (19), 195112.

64. Kim, S. C.; Kim, J. W.; Lee, J.; Park, Y., Formation of a Ca/LiF/Alq(3) cathode for an organic light-emitting diode: Evolution of the electronic structure as studied by photoemission spectroscopy. *Journal of the Korean Physical Society* **2008,** *53* (2), 812-817.

65. DeMasi, A.; Piper, L. F. J.; Zhang, Y.; Reid, I.; Wang, S.; Smith, K. E.; Downes, J. E.; Peltekis, N.; McGuinness, C.; Matsuura, A., Electronic structure of the organic semiconductor Alq3 (aluminum tris-8-hydroxyquinoline) from soft x-ray spectroscopies and density functional theory calculations. *The Journal of Chemical Physics* **2008,** *129* (22), 224705.

66. Abdou, M. S. A.; Orfino, F. P.; Son, Y.; Holdcroft, S., Interaction of Oxygen with Conjugated Polymers: Charge Transfer Complex Formation with Poly(3-alkylthiophenes). *Journal of the American Chemical Society* **1997,** *119* (19), 4518-4524.

67. Di Pietro, R.; Fazzi, D.; Kehoe, T. B.; Sirringhaus, H., Spectroscopic Investigation of Oxygen- and Water-Induced Electron Trapping and Charge Transport Instabilities in n-type Polymer Semiconductors. *Journal of the American Chemical Society* **2012,** *134* (36), 14877-14889.

68. Karmilov, A. Y.; Sysoeva, N. A.; Buchachenko, A. L., Complexes of molecular oxygen with organic ligands. *Journal of Structural Chemistry* **1978,** *18* (5), 649-654.

69. Zhang, R. Q.; Lee, C. S.; Lee, S. T., Effect of charging on electronic structure of the Alq3 molecule: the identification of carrier transport properties. *Chemical Physics Letters* **2000,** *326* (5–6), 413-420.

70. Curioni, A.; Boero, M.; Andreoni, W., Alq3: ab initio calculations of its structural and electronic properties in neutral and charged states. *Chemical Physics Letters* **1998,** *294* (4), 263-271.

71. Zhan, Y. Q.; de Jong, M. P.; Li, F. H.; Dediu, V.; Fahlman, M.; Salaneck, W. R., Energy level alignment and chemical interaction at Alq3/Co interfaces for organic spintronic devices. *Physical Review B* **2008,** *78* (4), 045208.

72. Riminucci, A.; Prezioso, M.; Pernechele, C.; Graziosi, P.; Bergenti, I.; Cecchini, R.; Calbucci, M.; Solzi, M.; Dediu, V. A., Hanle effect missing in a prototypical organic spintronic device. *Applied Physics Letters* **2013,** *102* (9).

73. Sun, X.; Gobbi, M.; Bedoya-Pinto, A.; Txoperena, O.; Golmar, F.; Llopis, R.; Chuvilin, A.; Casanova, F.; Hueso, L. E., Room-temperature air-stable spin transport in bathocuproine-based spin valves. *Nature Communications* **2013,** *4*, 2794.

74. Yu, Z. G., Impurity-band transport in organic spin valves. *Nat Commun* **2014,** *5*.

75. Hueso, L. E.; Pruneda, J. M.; Ferrari, V.; Burnell, G.; Valdes-Herrera, J. P.; Simons, B. D.; Littlewood, P. B.; Artacho, E.; Fert, A.; Mathur, N. D., Transformation of spin information into large electrical signals using carbon nanotubes. *Nature* **2007,** *445* (7126), 410-413.

76. Göckeritz, R.; Homonnay, N.; Müller, A.; Fuhrmann, B.; Schmidt, G., Resistive switching and voltage induced modulation of tunneling magnetoresistance in nanosized perpendicular organic spin valves. *AIP Advances* **2016,** *6* (4), 045003.

77. Santos, T. S.; Lee, J. S.; Migdal, P.; Lekshmi, I. C.; Satpati, B.; Moodera, J. S., Room-Temperature Tunnel Magnetoresistance and Spin-Polarized Tunneling through an Organic Semiconductor Barrier. *Physical Review Letters* **2007,** *98* (1), 016601.

78. Zhang, X.; Mizukami, S.; Ma, Q.; Kubota, T.; Oogane, M.; Naganuma, H.; Ando, Y.; Miyazaki, T., Spin-dependent transport behavior in C60 and Alq3 based spin valves with a magnetite electrode (invited). *Journal of Applied Physics* **2014,** *115* (17), 172608.

79. Galbiati, M.; Tatay, S.; Delprat, S.; Khanh, H. L.; Servet, B.; Deranlot, C.; Collin, S.; Seneor, P.; Mattana, R.; Petroff, F., Is spin transport through molecules really occurring in organic spin valves? A combined magnetoresistance and inelastic electron tunnelling spectroscopy study. *Applied Physics Letters* **2015,** *106* (8), 082408.

80. O'Shea, K. J.; MacLaren, D. A.; McGrouther, D.; Schwarzbach, D.; Jungbauer, M.; Hühn, S.; Moshnyaga, V.; Stamps, R. L., Nanoscale Mapping of the Magnetic Properties of (111)-Oriented La0.67Sr0.33MnO3. *Nano Letters* **2015,** *15* (9), 5868-5874.

TOC GRAPHIC

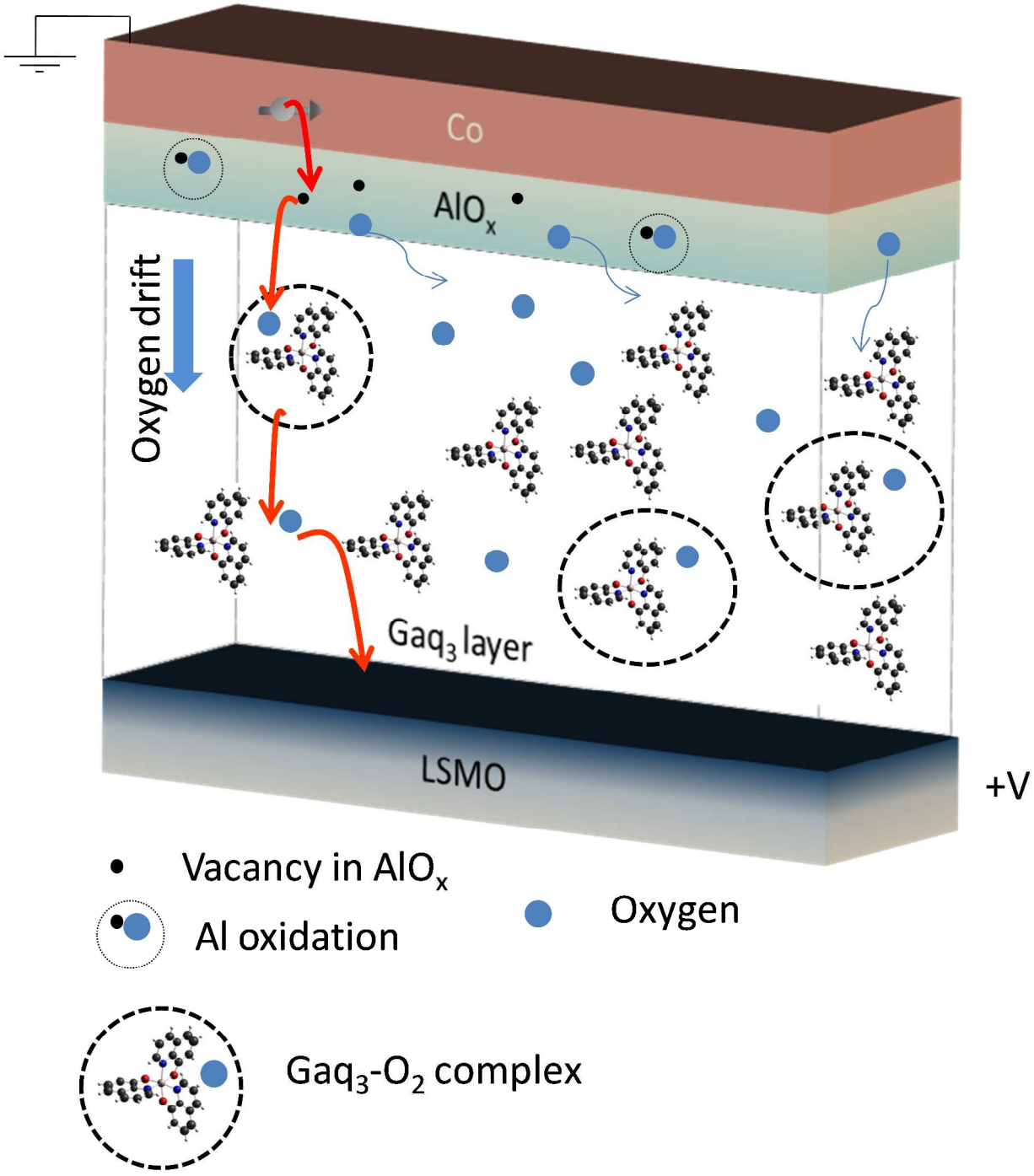
Co
AlO$_x$
Oxygen drift
Gaq$_3$ layer
LSMO
+V
Vacancy in AlO$_x$
Oxygen
Al oxidation
Gaq$_3$-O$_2$ complex

Supplementary information

S1:Voltage dependence of the hopping conductance

Figure S1, black dots, shows the differential conductance G as a function of the applied voltage in the HRS, top panel, and in the LRS, bottom panel. G is not constant, which rules out ohmic conduction. The amorphous nature of the Gaq3 and AlOx barriers indicated that charge transport could be understood in terms of the model by Xu et al. [1]. According to this model, the conductance G could be described by a voltage dependent expression in which each V^x represents a different charge transport channel:

$$Ga(V)= G_0+G_{4/3}\times V^{4/3}+G_{5/2}\times V^{5/2}$$

where G_0includes both direct and resonant tunneling, $V^{4/3}$ describes hopping across two impurity states in the amorphous insulating barrier, while $V^{5/2}$ describes hopping across 3 impurity states.In order to explain the asymmetry of G, we also introduced a linear term in V, which represents the contribution of asymmetric injection barriers from the electrodes [2]

$$G(V)= G_0+ G_{LIN}\times V+G_{4/3}\times V^{4/3}+G_{5/2}\times V^{5/2}$$

The red curves in Figure S1 represent the fit, which are in excellent agreement with the data for both resistive states. This demonstrates that the conduction mechanism is the same in both states and that what changes between the two is the number of sites across which hopping is possible.

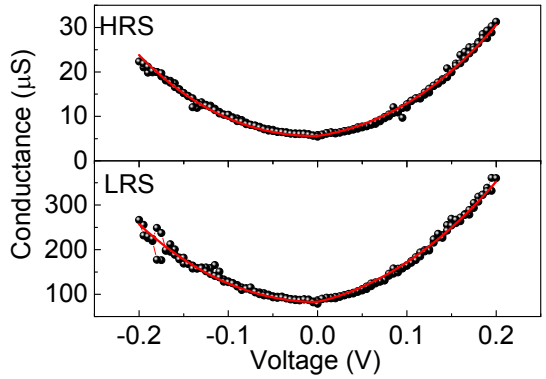

Figure S1: Differential conductance of a device at 300 K in HRS and LRS

S2:EELS analysis

Electron energy loss spectroscopy was used to assess compositional variations across the devices and typical results are presented in **Fig. S2**, the upper panels of which (b) indicate the distribution of elements within the dotted region of Fig. S2(a). The EELS signals reveal the clear laminar structure and reveal in particular the oxygen band beneath the top Co electrode that is consistent with the presence of a continuous AlO_x barrier layer. The elemental distribution as a function of depth is more clearly plotted in Fig. S2(c), which plots the integrated elemental counts within the upper panels. (Note that uneven milling during the FIB preparation has led to the thickness of the organic layer appearing wedge-like in the N signal.) Of particular note is the uniform oxygenation of the organic layer, which is implicated in the switching mechanism proposed below. Note, also, that the Co signal does not stop abruptly at the upper AlO_x interface, but tails-off across the AlOx and into the organic layer. More detailed analysis of the Co $L_{2,3}$ signal, shown in Fig. S2(d) and S2(e), indicates the trace quantities of Co within the AlO_x and organic layers to be oxidized: the concentration of oxide is too low to give rise to a strong signal in the HAXPES results described below.

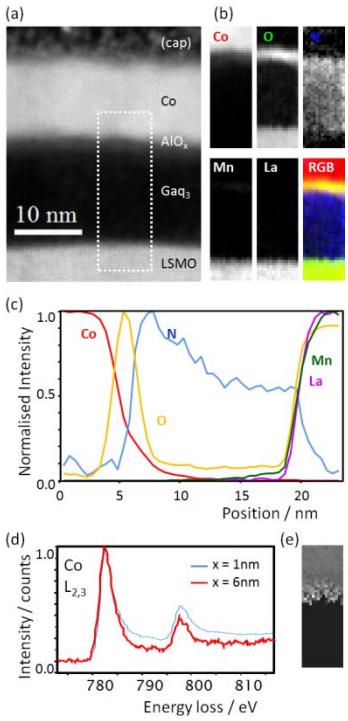

Fig. S2. Electron energy loss spectroscopic analysis of a typical device. (a) Dark field STEM image with major layers labeled. Heavier elements appear darkest and the region used for EELS analysis is indicated. (b) Composition maps showing the distribution of elements within the analysed region,

each panel indicating the relative strength of background-subtracted EELS signal. The final panel is a red-green-blue composite of the Co, O and N signals. (c) Line profiles derived from the composition maps, showing the distribution of elements across the device. Note that uneven FIB milling of the organic layer leads to the apparent wedge-shaped nitrogen profile. (d) Detail of the Co $L_{2,3}$ EELS edges taken within the electrode and at the position of the AlO_x barrier, where small quantities of oxidized Co are found. (e) A map of the change in the $L_{2,3}$ integrated intensity ratio is consistent with oxidation of the intermixed Co, within the barrier region.

S3: O Kedge XAS interpretation:

From [3] and reference therein, O K-edge lineshape for amorphous AlOx layers, as expected in our case and confirmed by TEM, is constituted by one broad peak and at least 2 low intensity features far from the main peak (ΔE1= 4.7 eV and ΔE2=10 eV). From the satellite energy position, we can associate the exact spectra position of O K-edge for AlO_x by locating the small feature at 531.3 eV as the peak at ΔE2. As consequence the peak ΔE1 is associated to peak A. The contribution of Gaq3 to O K-edge consists of a main broad peak with two satellites with separation ΔE=1.5eV associated to transition from O1s to respectively LUMO, LUMO+1 (taken from refs [4] [5]). The relative energy separation between peak B and A (Δ(B-A)= 2.8 eV) is larger than that associated to the Gaq3 satellites, making thus the association of the A peak univocally to AlO_x.

S4: XPS Al1s

Al 1s peak consists of three components that we associate to Al oxide (AlO_x) , to elemental Al and to higher oxidation states for Al, as for example Al2O3 contributions [6]. Each contribution is fitted by using a Guassian line shape. The following table summarizes the assignments and the relative contribution to the total peak area in the three resistive states.

	Assignement	Energy (eV)	FWHM	Peak area
IRS	Al-O	1561.2	1.7	62.0 %
	Al-Al	1558.6	2.5	14.5%
HRS	Al-O	1561.3	1.8	78.0%
	Al-Al	1558.6	2.0	5.5%
LRS	Al-O	1561.1	1.6	74.0%
	Al-Al	1558.6	3.1	8.1%

References

[1] Y. Xu, D. Ephron, M. R. Beasley, *Physical Review B* **1995**, 52, 2843.

[2] W. F. Brinkman, R. C. Dynes, J. M. Rowell, *Journal of Applied Physics* **1970**, 41, 1915.

[3] C. Århammar, A. Pietzsch, N. Bock, E. Holmström, C. M. Araujo, J. Gråsjö, S. Zhao, S. Green, T. Peery, F. Hennies, S. Amerioun, A. Föhlisch, J. Schlappa, T. Schmitt, V. N. Strocov, G. A. Niklasson, D. C. Wallace, J.-E. Rubensson, B. Johansson, R. Ahuja, *Proceedings of the National Academy of Sciences* **2011**, 108, 6355.

[4] T. Yokoyama, H. Ishii, N. Matsuie, K. Kanai, E. Ito, A. Fujimori, T. Araki, Y. Ouchi, K. Seki, *Synthetic Metals* **2005**, 152, 277.

[5] S. Fang, Z. Pang, Y. Du, L. Zheng, X. Zhang, F. Wang, H. Yuan, S. Han, *Journal of Applied Physics* **2012**, 112, 113519.

[6] P. Risterucci, O. Renault, C. Zborowski, D. Bertrand, A. Torres, J. P. Rueff, D. Ceolin, G. Grenet, S. Tougaard, *Applied Surface Science* **2017**, 402, 78.